On the identification of substructure in phase space using orbital frequencies

Gomez, Facundo A.; Helmi, Amina

Published in:
Monthly Notices of the Royal Astronomical Society

DOI:
10.1111/j.1365-2966.2009.15841.x

Monthly Notices of the ROYAL ASTRONOMICAL SOCIETY

Mon. Not. R. Astron. Soc. **401,** 2285–2298 (2010) doi:10.1111/j.1365-2966.2009.15841.x

On the identification of substructure in phase space using orbital frequencies

Facundo A. Gómez★ and Amina Helmi

Kapteyn Astronomical Institute, University of Groningen, PO Box 800, 9700 AV Groningen, the Netherlands

Accepted 2009 October 5. Received 2009 October 5; in original form 2009 April 8

ABSTRACT

We study the evolution of satellite debris to establish the most suitable space to identify past merger events. We confirm that the space of orbital frequencies is very promising in this respect. In frequency space individual streams can be easily identified, and their separation provides a direct measurement of the time of accretion. We are able to show for a few idealized gravitational potentials that these features are preserved also in systems that have evolved strongly in time. Furthermore, this time evolution is imprinted in the distribution of streams in frequency space. We have also tested the power of the orbital frequencies in a fully self-consistent (live) *N*-body simulation of the merger between a disc galaxy and a massive satellite. Even in this case, streams can be easily identified and the time of accretion of the satellite can be accurately estimated.

Key words: methods: analytical – methods: *N*-body simulations – galaxies: formation – galaxies: kinematics and dynamics.

1 INTRODUCTION

In the current standard cosmological model, known as Λ cold dark matter, galaxies like our own Milky Way are formed bottom-up, through the merger and accretion of smaller building blocks that come together due to their gravitational attraction (e.g. White & Rees 1978).

This model is being continuously tested and many questions and puzzles remain to be addressed. An example is the large number of bound substructures predicted to orbit galaxies like the Milky Way and M31 compared to the observed abundance of satellite galaxies in these systems (Klypin et al. 1999; Moore et al. 1999), although several solutions have been proposed (e.g. Bullock, Kravtsov & Weinberg 2000). The formation of realistic disc galaxies in full cosmological simulations remains another great challenge (e.g. Steinmetz & Navarro 1999) yet steady progress is being made (e.g. Governato et al. 2004, 2007; Scannapieco et al. 2009).

One strong test of the current paradigm may be performed through observations of the stellar haloes of galaxies like the Milky Way. For example, if the Galaxy was formed in a hierarchical fashion via mergers then we should be able to find fossil signatures of these events in the present-day phase-space distribution of halo stars. This idea was strongly exalted after the discovery of the disrupting Sgr dwarf galaxy by Ibata, Gilmore & Irwin (1994). In the following years, further debris from accretion events was discovered, not only in the halo (Helmi et al. 1999; Grillmair 2006; Belokurov et al. 2006) but also in the disc of our Galaxy (Eggen 1996; Ibata et al. 2003; Yanny et al. 2003; Navarro, Helmi & Freeman 2004; Helmi et al. 2006), although some of this substructure may be of dynamical origin (Antoja et al. 2009; Minchev et al. 2009).

However, if the hierarchical scenario is correct, we are still far from having unveiled every single stream associated to each merger event the Galaxy has experienced in its lifetime. Helmi, White & Springel (2003) by combining numerical simulations with analytic work predicted that there should be several hundreds of cold stellar streams present in the vicinity of the Sun (see also Vogelsberger et al. 2008). The short dynamical time-scales, especially in the solar neighbourhood, are the basic reason behind why such a large number is expected. An accreted satellite, orbiting in the inner regions of the Galaxy, will give rise to multiple stellar streams in a relatively short period of time. As shown by Helmi & White (1999), the spatial density of these streams is a strongly decreasing function of time. Consequently, substructure associated to a past accretion event is expected to have a very low-density contrast, making its detection very difficult from its distribution in space. On the other hand, due to the conservation of phase-space density, the velocity dispersion of a stream will decrease as time goes by, making the streams tighter in the velocity domain.

The arguments above highlight the need for full six-dimensional phase-space information to completely disentangle the predicted wealth of substructure. Furthermore, samples of at least 1000 halo stars would appear to be necessary for this enterprise. Statistical arguments using the revised New Luyten Two Tenths proper motion survey (Gould & Salim 2003; Salim & Gould 2003) have been used to measure the amount of granularity (associated to moving groups) in the stellar halo near the Sun. Gould (2003) has shown that no

★E-mail: gomez@astro.rug.nl

streams are present in this region of the Galaxy that contain more than approximately 5 per cent of the halo stars near the Sun. This estimate is in good agreement with the expectations described above, but does not provide a direct confirmation of the predictions. Spectroscopic surveys such as the Radial Velocity Experiment (RAVE) (Zwitter et al. 2008) and the Sloan Extension for Galactic Understanding and Exploration (SEGUE) (Yanny et al. 2009) should be helpful in identifying further nearby streams (e.g. Smith et al. 2009; Klement et al. 2009) but the breakthrough will take place only with the astrometric satellite *Gaia* (Perryman et al. 2001). *Gaia*, expected to be launched in 2011, will measure the positions and motions of 10^9 stars with very high accuracy.

Given the datasets that soon will become available it is natural to ask what is the optimal way to discover merger debris. More precisely, the question we would like to address in this work is what is the best space to look for substructure if our goal is to disentangle how the Galaxy was assembled.

The first steps in this direction have been presented by Helmi & de Zeeuw (2000). These authors analysed simulations of the disruption of satellite galaxies in a fixed Galactic potential and concluded that the 'integrals-of-motion' space defined by the energy, the total angular momentum and its z-component (E, L, L_z) is very suitable for identifying the remains of past accretion events. Even in fully self-consistent cosmological simulations, disrupted satellites still appear as coherent structures in this 'integrals-of-motion' space (Knebe et al. 2005). Font et al. (2006) demonstrated the power of complementary chemical abundance information to disentangle debris from different events. Arifyanto & Fuchs (2006) have used for samples of nearby stars the space defined by $(U^2 + 2V^2)^{1/2}$ and V, where U is the radial velocity in the Galactic plane and V is the velocity component in the direction of rotation. More recently, McMillan & Binney (2008) (hereafter MB08) showed that action-angle coordinates and in particular the orbital frequencies could conform a very convenient set of variables to identify nearby substructure.

In this paper, we explore further the power of the orbital frequencies. We start our journey by briefly reviewing the concept of action-angle variables in Section 2. In Section 3, we discuss in depth the space of orbital frequencies. We characterize the distribution of debris in a few simple cases and in particular in a static spherical potential. In Section 4, we analyse how the structure of this space is altered in a time-dependent (still rigid) potential. Finally, in Section 5 we focus on a live N-body simulation of the accretion of a massive satellite on to a pre-existing thin disc. We discuss and summarize our results in Section 6.

2 THE ACTION-ANGLE VARIABLES

Let us consider a dynamical system with a time-independent Hamiltonian $H(\boldsymbol{p}, \boldsymbol{q})$, where $(\boldsymbol{p}, \boldsymbol{q})$ is a set of $2n$ canonical coordinates. The dynamical state of this system is governed by the Hamilton's equations

$$\dot{p}_i = -\frac{\partial H}{\partial q_i}, \qquad \dot{q}_i = \frac{\partial H}{\partial p_i}, \tag{1}$$

with $i = 1, \ldots, n$.

The evolution of a system may be expressed much more simply by performing a canonical transformation of coordinates such that the equations of motion are

$$\dot{P}_i = -\frac{\partial H(\boldsymbol{P})}{\partial Q_i} = 0, \qquad \dot{Q}_i = \frac{\partial H(\boldsymbol{P})}{\partial P_i} = \Omega_i(\boldsymbol{P}), \tag{2}$$

with solutions

$$Q_i = Q_i^0 + \Omega_i t, \qquad P_i = P_i^0. \tag{3}$$

If the system under study is such that the motion is periodic then this set of canonical variables is known as action-angle variables.

In a spherical potential $\Phi(r)$, the radial action is

$$J_r = \frac{1}{\pi}\int_{r_1}^{r_2} \mathrm{d}r \frac{1}{r}\sqrt{2[E - \Phi(r)]r^2 - L^2}, \tag{4}$$

where L is the total angular momentum, r_1 and r_2 the turning points in the radial direction and

$$J_\phi = L_z, \qquad J_\theta = L - L_z \tag{5}$$

are the angular actions. The frequencies of motion $\Omega_i = \partial H/\partial J_i$ can be derived by differentiation of the implicit function

$$g = J_r - \frac{1}{\pi}\int_{r_1}^{r_2} \mathrm{d}r \frac{1}{r}\sqrt{2[E - \Phi(r)]r^2 - L^2} \tag{6}$$

defined by equation (4). For more details, see e.g. Goldstein, Poole & Safko (2001).

3 FREQUENCY SPACE FOR STATIC POTENTIALS

3.1 Toy-model

The space of orbital frequencies in the context of isolating debris from accreted satellites was first introduced by MB08. For completeness, we here review its main characteristics. We also refer the reader to section 4 of MB08. For this purpose, we have developed a simple toy-model and followed the evolution of a satellite in this space.

Let us consider a satellite (i.e. a system of particles that are initially strongly clustered in phase space) orbiting under the influence of an arbitrary gravitational potential. For simplicity, we consider a system with only two independent frequencies of motion. We will also assume that the initial distribution in action-angle space of the satellite follows a multivariate Gaussian with dispersions of $\sigma_\theta = \pi/4$ and $\sigma_J = \pi/3$ in the angles and actions, respectively (and no correlation among the different directions). In this space, the location of a given particle will vary only due to the evolution of the angle coordinates. The rate of evolution, i.e. the frequencies, is completely determined by the underlying potential in which our satellite evolves (see equation 3). The other two coordinates, i.e. the actions, will remain constant in time.

Here, we will assume that we can express the frequencies in the following way:

$$\begin{aligned}\Omega_1 &= c_1 J_1 + c_2 J_2,\\ \Omega_2 &= c_3 J_1 + c_4 J_2,\end{aligned} \tag{7}$$

where c_i are constants. In general, the relation between the frequencies and the actions is more complex, and depends on the specific form of the gravitational potential.

Typically, we have access to samples of stars located in a particular region of space such as, for example, the solar neighbourhood. This constraint acts as a filter, implying that we only observe the subset of stars with orbital properties such that they are in this particular location at the time of observation. To mimic this, we focus on the particles located in a small region of the angles' space in our toy-model. Fig. 1 shows the distribution of these particles in the space of actions and of frequencies at three different times ($0 < t_1 < t_2 < t_3$).

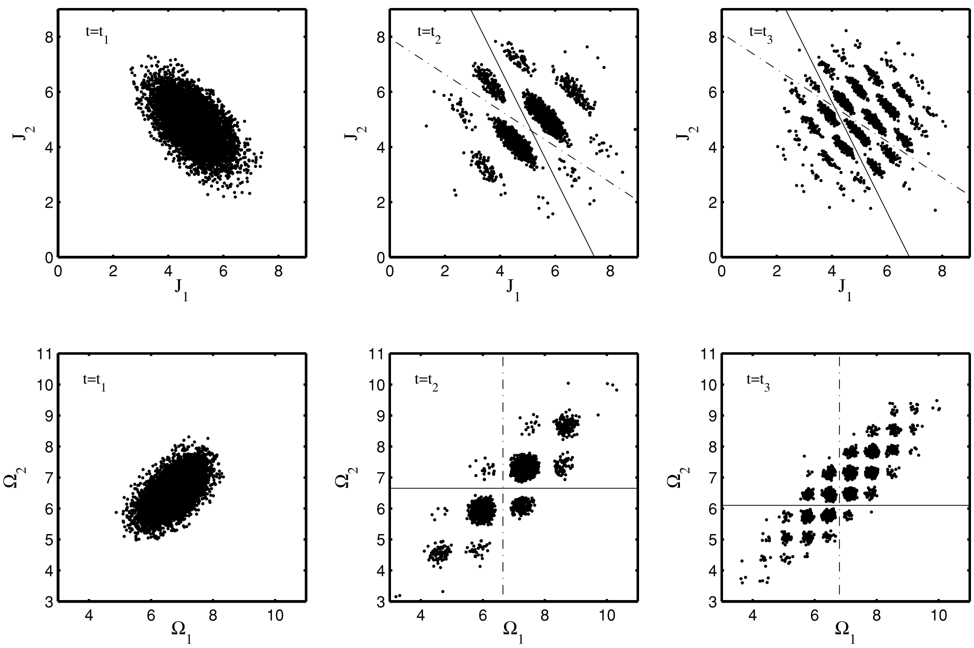

Figure 1. Distribution of particles in actions (upper panels) and frequency (lower panels) space located in a small region of the angle space at three different times. Each clump represents a particular stream crossing this region at the time considered. The solid lines indicate Ω_2 = constant whereas the dot–dashed lines represent lines of constant Ω_1, as shown in the bottom panels.

As discussed by MB08, the particles passing through a particular location of (angle-)space are distributed in different patches or streams. With time, the number of streams increases while their extent in frequency space decreases. When the particles cross our location for the first time, they have not had enough time to become significantly spread in angle. We then observe only one big stream (left-hand panel of Fig. 1). At some later time, particles with the highest frequencies begin to overtake the slowest ones and therefore we observe multiple streams (since the angles are periodic) each with its own characteristic frequency. The size of each individual stream at any given time is dependent on the size of the small region under consideration and on the initial spread of the system.

Since the orbital frequencies are constant (for a time-independent gravitational potential), the location of a particle in frequency space remains unchanged. The changing pattern shown in Fig. 1 is simply a consequence of the fact that we restrict our analysis to particles at a given spatial location. The gaps thus correspond to particles which are located outside our window.

The network of patches is shaped by lines of constant frequency Ω_i = constant. As a consequence, and because of the relation implied by equation (7), the distribution of particles in action space is also very regular. However, in general the relation between frequencies and actions will not be linear, and therefore the distribution of particles in action space is typically more complex (see e.g. Fig. 5).

The number of clumps observed along each frequency direction at a given location can be estimated by considering the initial spread in the frequency. For example, at Ω_2 = constant, $\Delta\Omega_1 = \Omega_1^{\max} - \Omega_1^{\min}$. After some time $t = t_3$, the angle θ_1 between the particles with the largest and smallest Ω_1 has increased to

$$\Delta\theta_1(t_3) = \Delta\Omega_1 t_3 + \Delta\theta_1(t_0). \tag{8}$$

with $\Delta\theta_1(t_0)$ the initial separation at time t_0. Since θ_1 is a 2π-periodic variable, the number of streams N_1 at Ω_2 = constant is

$$N_1 = \left[\frac{\Delta\theta_1(t_3)}{2\pi}\right] = \left[\frac{\Delta\Omega_1 t_3 + \Delta\theta_1(t_0)}{2\pi}\right] \approx \left[\frac{\Delta\Omega_1 t_3}{2\pi}\right], \tag{9}$$

where the last approximation holds if t_3 is long enough such that $\Delta\Omega_1 t_3 \gg \Delta\theta_1(t_0)$.

Another quantity of interest is the distance between two adjacent streams in frequency space,

$$\delta\Omega_i = \frac{\Delta\Omega_i}{N_i} \approx \frac{2\pi}{t}, \qquad i = 1, 2. \tag{10}$$

The time t may be considered as the time since disruption of our system (i.e. its constituent stars have been tidally stripped, and move only under the influence of the host gravitational field). Equation (10) states that this time can be directly estimated by measuring $\delta\Omega_i$. Moreover, systems will have different values of $\delta\Omega_i$ depending on the time since disruption, which implies that this characteristic scale could be used to recognize the streams originating in objects plausibly accreted at different epochs.

3.2 Spherical potentials

We now consider dynamical systems with an underlying spherical potential, $\Phi(r)$. Due to the conservation of angular momentum L, the motion of stars are constrained to remain in a plane, implying that there are only two independent frequencies of motion: Ω_r associated to the radial oscillation and Ω_ϕ associated to the angular oscillation in this plane.

3.2.1 Characterising frequency space

Our previous analysis has shown that the space of frequencies appears to be well suited to identify streams. Here we will characterise this space and how its properties depend on the form of the host gravitational potential.

The angular and radial periods of an orbit are related to the respective frequencies through

$$T_\phi = 2\pi/\Omega_\phi, \quad T_r = 2\pi/\Omega_r. \tag{11}$$

Once a radial oscillation is completed, the azimuthal angle has increased by an amount $\Delta\phi = \Omega_\phi T_r$ or, equivalently

$$\Delta\phi = 2\pi \frac{\Omega_\phi}{\Omega_r},$$

thus

$$\frac{\Omega_r}{\Omega_\phi} = \frac{T_\phi}{T_r} = \frac{2\pi}{\Delta\phi}. \tag{12}$$

In general, $2\pi/\Delta\phi$ will not be a rational number and therefore the orbit will not be closed. However, there are two gravitational potentials in which all orbits are closed, those of an homogeneous sphere and of a point mass. Note that any other spherical system may be considered to have a mass distribution between these limiting cases, i.e. its density gradient will be neither as shallow nor as steep as in these two cases. Orbits in a time-independent homogeneous mass distribution have $\Delta\phi = \pi$, whereas for the Kepler problem $\Delta\phi = 2\pi$. From Equation (12), this implies that the frequencies of a bound orbit in any spherical mass distribution are constrained to lie inside the subspace defined by $\Omega_r/2 \leq \Omega_\phi \leq \Omega_r$. The extent to which this subspace is probed by orbits depends on the exact distribution of mass. To examine this, let us consider the Plummer potential, Φ, generated by a density ρ, where

$$\Phi(r) = \frac{-GM}{\sqrt{r^2 + b^2}},$$

$$\rho(r) = \frac{3M}{4\pi b^3}\left(1 + \frac{r^2}{b^2}\right)^{-5/2} \tag{13}$$

(Plummer 1911). We sample the frequency space in this potential by randomly drawing 10^4 orbits from the distribution function associated to the Plummer sphere with parameters $M = 10^{12}\,\mathrm{M}_\odot$ and $b \approx 22$ kpc. The upper panel in Fig. 2 shows the distribution of these orbits in frequency space. The solid line and dashed lines correspond to $\Omega_r = 2\Omega_\phi$ (homogeneous sphere) and $\Omega_r = \Omega_\phi$ (point mass), respectively. Note that orbits with small frequencies cover the whole region between these two lines. Instead, orbits with high frequencies tend to bend over towards the line given by the homogeneous sphere. This is because particles on orbits with low frequencies populate the outer regions of the system, and hence perceive a potential close to that of a point mass. On the other hand, those on high-frequency orbits are generally confined to the central regions of the system. Since the Plummer density profile has a core, these particles will feel a potential resembling that of the homogeneous distribution. The strict cut-off at a value of $\Omega_r \approx 42$ Gyr^{-1} therefore corresponds to the characteristic frequency associated to the homogeneous mass distribution, i.e. for $r << b$ a particle in the Plummer model should have a period of $T_r \sim \sqrt{\frac{\pi^2 b^3}{GM}}$ which in our case corresponds to 0.15 Gyr, or $\Omega_r = 42$ Gyr^{-1}.

For a given Ω_ϕ, (nearly) circular orbits will be those with the largest radial period, i.e. the smallest Ω_r frequency. Thus, such orbits are located on the wedge seen in the top panel of Fig. 2. This is also illustrated in the bottom panel of the same figure, where we have plotted the ratio of apocentre to pericentre distances of orbits as a function of Ω_r. As we can see, orbits with the lowest Ω_r for a given $\Omega_\phi =$ constant have $r_{\rm apo}/r_{\rm per} = 1$.

We now consider a system with a cuspy density distribution, namely the Hernquist profile whose potential, Φ, and density, ρ, are given by

$$\Phi(r) = \frac{-GM}{r + b},$$

$$\rho(r) = \frac{bM}{2\pi r}\frac{1}{(r + b)^3} \tag{14}$$

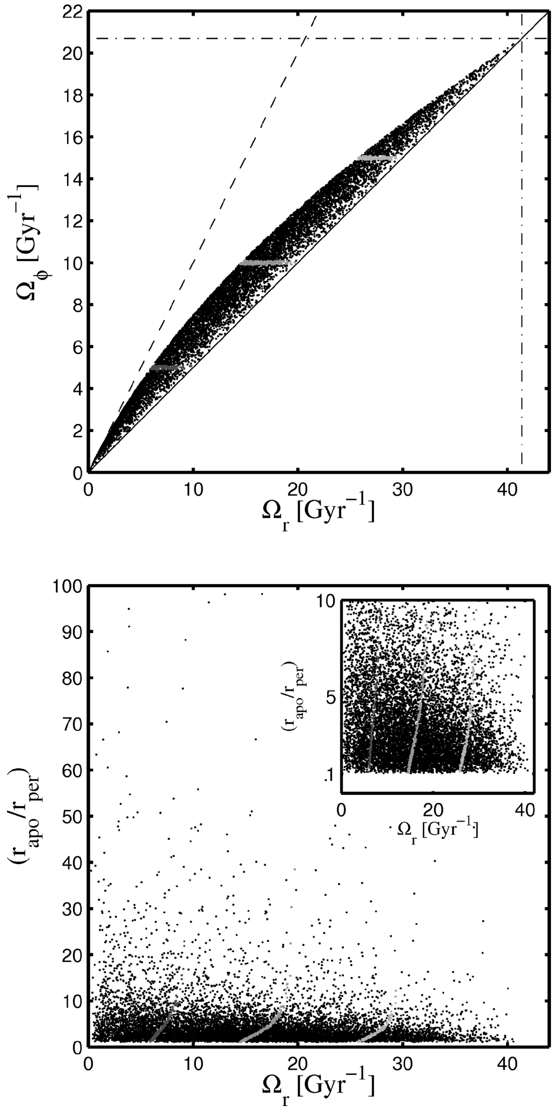

Figure 2. Top panel: distribution of possible orbits in a Plummer sphere in frequency space. The solid line corresponds to $\Omega_r = 2\Omega_\phi$, as in the case of orbits in a homogeneous sphere. The dashed line shows $\Omega_r = \Omega_\phi$, as found for all orbits in a point-mass distribution. The left wedge of the distribution corresponds to circular orbits. Bottom panel: relation between the radial frequency Ω_r and the orbital apocentre-to-pericentre ratio.

(Hernquist 1990). We set $M = 10^{12}\,\mathrm{M}_\odot$ and $b \approx 22$ kpc. As before, we sample the available phase space with 10^4 orbits. The black points in Fig. 3 show the resulting distribution of orbits in frequency space. For comparison, we overplotted the frequencies for the Plummer profile (in grey). At the low-frequency end, both distributions overlap as expected (point mass regime). However, there is a significant difference in the region populated by orbits with high frequencies. Due to the lack of a core in the Hernquist density distribution, the bend over towards $\Omega_r = 2\Omega_\phi$, i.e. the regime of the homogeneous mass distribution, has disappeared, and there is no upper limit to the radial or angular frequency of motion.

3.2.2 Comparing different projections of phase space

Various spaces have been proposed to identify debris from disrupted satellites. For example, Helmi & de Zeeuw (2000) introduced the

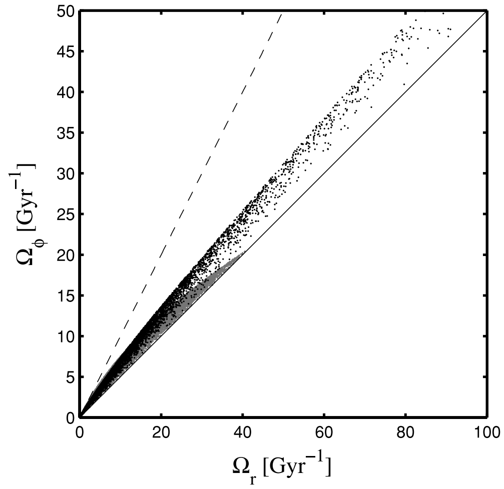

Figure 3. Distribution of possible orbits in a Hernquist profile (black dots) in frequency space. For comparison, the distribution for a Plummer sphere is shown in grey. Solid and dashed lines represent as before the natural limits of this space, i.e. $\Omega_r = 2\Omega_\phi$ and $\Omega_r = \Omega_\phi$, respectively. Note that because the Hernquist inner density profile is cusped orbits with high frequencies do not bend over to the boundary associated with the homogeneous sphere.

space of energy, total angular momentum and its z-component (E, L, L_z). Later on, Helmi et al. (2006) showed that substructure can be identified by looking at the apocentre, pericentre and L_z space. In this space, streams are represented by extended structures, roughly along a line of constant eccentricity. In this section, we will compare the distribution of debris in these and other previously used spaces to that in frequency space. To this end, we consider the accretion of a satellite galaxy on to a spherical host.

We represent the host with the Plummer profile discussed in the previous section. The satellite is assumed to be spherical and to have an isotropic velocity ellipsoid, and is modelled with a multivariate Gaussian in 6D with a dispersion of $\sigma_x \approx 1$ kpc and $\sigma_v = 22$ km s^{-1}. We set the central particle of the satellite on an orbit with apocentre $r_{\rm apo} \approx 35$ kpc, pericentre $r_{\rm per} \approx 8$ kpc and inclined by 56° with respect to the z-axis. We follow then the evolution of the satellite for approximately 10 Gyr. For simplicity, in this experiment the self-gravity of the satellite is not considered. As a consequence, we expect to find a larger number of streams at any given epoch, with a larger spread in orbital parameters, in comparison to the self-gravitating case. This is because particles can drift apart from each other right from the start, whereas when their self-gravity is considered, this will only happen during successive pericentric passages where they are (typically) stripped from the parent satellite.

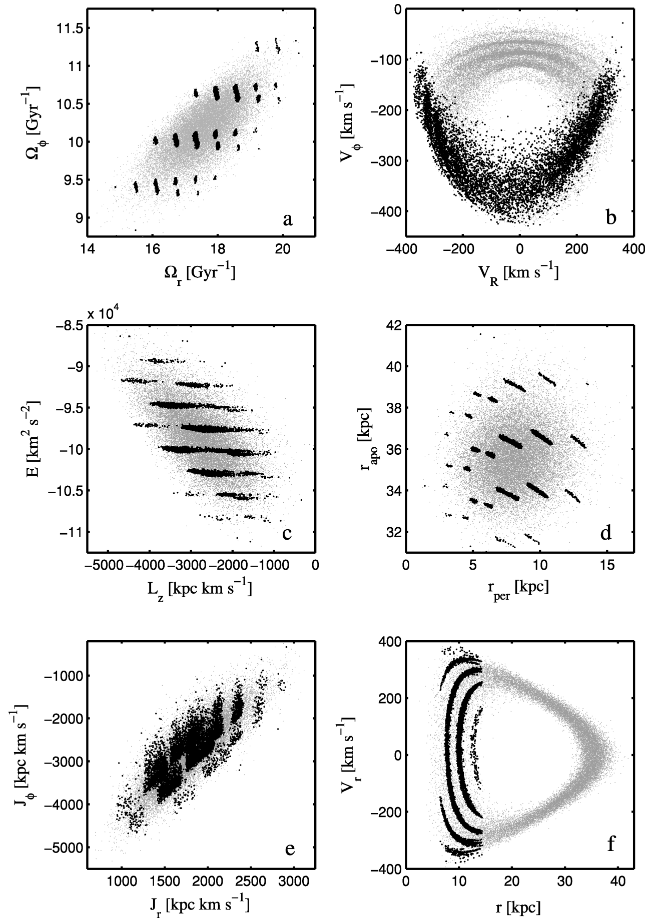

Figure 5. Comparison of the various spaces commonly used to identify merger debris. Grey dots show the distribution of all satellite particles whereas the black dots represent the particles inside the sphere shown in Fig. 4. As in the toy model example discussed in Section 3.1, streams in frequency space (top-left panel) are distributed in a regular pattern. Note that the distribution of particles in frequency space is much better defined than in any other of the spaces considered.

In Fig. 4, we show the spatial distribution of satellite particles at three different times. To study the distribution of particles in various projections of phase space, we focus on those inside an sphere of radius 4 kpc centred at $r \approx 10$ kpc at the final time, as shown in the rightmost panel of this figure.

The results are shown in Fig. 5 for six different spaces. Grey points represent all the particles of the satellite whereas black

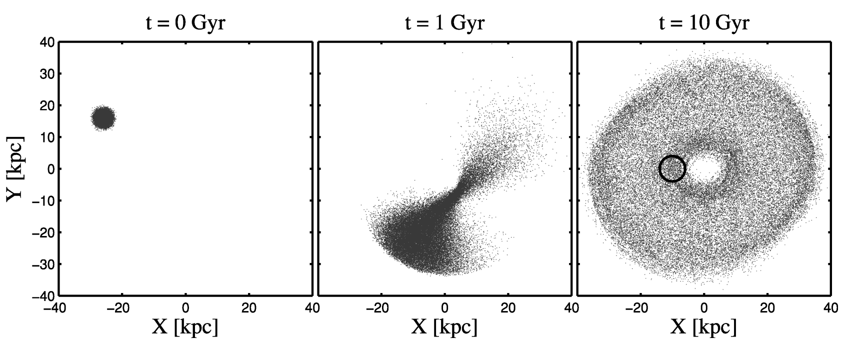

Figure 4. $X - Y$ distribution of particles from an accreted satellite at three different times, as indicated on each panel. The black circle shows the location of a 'solar neighbourhood' sphere.

points only those inside the sphere of interest. In the top-left corner (panel a), we show their projection in frequency space. As in the toy model discussed in Section 3.1, for a given Ω_ϕ = constant we find multiple streams in Ω_r. Note that there are typically more streams at constant Ω_ϕ than at constant Ω_r. This is because $T_r \leq T_\phi \leq 2T_r$, and hence mixing occurs faster in the r-direction.

Note that some of the groups of particles found at given Ω_r and $\Omega_\phi \approx$ constant may be decomposed into smaller structures. This can be understood from the radial velocity versus radial distance plot shown in the bottom-right panel of Fig. 5. Streams with pericentres inside the sphere under consideration appear in frequency space as a single compact structure. For the rest, we observe two separate structures, each of these associated to particles located just before or after their corresponding pericentre.

The top-right panel of Fig. 5 shows the distribution of particles in a projection of velocity space. Although several features are visible, the individual streams are clearly less well separated than in panel a). This is also the case for the radial velocity versus radial distance plot (panel f).

The two middle panels of Fig. 5 show the distribution of particles in the $E-L_z$ (left-hand panel) and apocentre versus pericentre (right-hand panel) spaces. The number of structures in the $E-L_z$ space is smaller and slightly less sharp than in frequency space. On the other hand, streams are well detached from each other in the apocentre versus pericentre space. Finally, in the bottom-left panel we show the distribution of particles in the space of actions, J_r versus J_ϕ. As in the $E-L_z$ space, distinction of the various streams is less clear in this space, and hence it appears to be less suitable for finding individual debris streams. However, it is important to note that we are only considering two of the three available actions. By projecting the particle's distribution into the principal directions of action space, it is also possible to find a well-defined distribution of streams (see fig. 7 of MB08).

This analysis shows that frequency space is a very suitable space to identify streams associated to accretion events. Moreover, as we explained in Section 3.1, the way streams are distributed in this space can allow us to estimate quantities such as time since disruption. This last characteristic makes the space of orbital frequencies more appealing than the other spaces previously considered.

3.2.3 Estimating the time of accretion

As discussed before, the separation between adjacent streams along each direction of the space of orbital frequencies yields a direct estimate of the time since disruption, e.g. a satellite accreted 10 Gyr ago should give rise to streams separated by a scale $\delta\Omega_r = \delta\Omega_\phi = 2\pi/10\,\mathrm{Gyr}^{-1}$.

By considering information from the distribution of particles not only in frequency but also in angle space, MB08 developed a powerful method that, by a process of iteration over a guess potential, allows to estimate time of disruption and to pin down the true underlying potential.

In this section, we explore a different method which, only based on the regularity seen in frequency space, provides an accurate estimate of time since disruption. As an example, we focus on the streams shown in panel (a) of Fig. 5. Because there is a unique scale (all streams are separated by the same amount), a straightforward way to compute the separation between adjacent streams is to use Fourier analysis techniques. We proceed by first creating an image from the scatter plot in frequency space, to which we then apply a Fourier transform. In the final step, we compute the power spectrum. To obtain an image from our data, we grid the frequency space with a regular $N \times N$ mesh of bin size Δ in both Ω_r and Ω_ϕ directions. In this way, the number of particles in the (n_r, n_ϕ) bin of the grid is $h(n_r, n_\phi)$. We apply a two-dimensional discrete Fourier transform to this image:

$$H(k_r, k_\phi) = \sum_{n_r=0}^{N-1}\sum_{n_\phi=0}^{N-1} \exp(2\pi \mathrm{i} k_r n_r/N) \exp(2\pi \mathrm{i} k_\phi n_\phi/N) h(n_r, n_\phi), \tag{15}$$

with $k_r, k_\phi = -\frac{N}{2}, \ldots, \frac{N}{2} - 1$.

In the top panel of Fig. 6, we show the image of the panel (a) of Fig. 5 in the Fourier space. This has been computed on a grid of 200 × 200 elements. The axes represent the wavenumbers in each direction $(k_r/(N\Delta), k_\phi/(N\Delta))$ while the colour coding show the square value of each of the Fourier components $|H(k_r, k_\phi)|^2$. As we can see from this image, and as expected from our previous discussion, a regular pattern is present. To measure the characteristic scale, we consider two different 'slits' (of 4 bin width) of the Fourier image around $k_r = 0$ and $k_\phi = 0$. These regions are delimited by the black lines in the top panel of Fig. 6. We can now compute the one-dimensional power spectrum of the image along each direction as

$$\begin{aligned} P(0) &= \frac{1}{N^2}\,|H(0,0)|^2\,, \\ P(k_r) &= \frac{1}{N^2}\left[|H(k_r,0)|^2 + |H(-k_r,0)|^2\right] \\ &\text{for } k_r = 1, \ldots, \left(\frac{N}{2} - 1\right), \\ P(N/2) &= \frac{1}{N^2}\,|H(-N/2,0)|^2 \end{aligned} \tag{16}$$

and analogously for $P(k_\phi)$. Recall that the one-dimensional power spectrum we compute is, in practice, an average over the slits considered along the k_r and k_ϕ directions.

The results are shown in the middle and the bottom panels of Fig. 6, for $P(k_r)$ and $P(k_\phi)$, respectively. The scales present in the power spectrum $P(k_r)$ are associated to separations in the Ω_r direction (since they correspond to $k_\phi = 0$). The large power for wavenumbers close to zero, i.e. $P(0)$ represents the average power over the whole image. All other peaks in the spectrum are related to waves resonating with our image. In particular, the first peak, with the highest power, is associated to a wavenumber of $f_0 = 1.59$ Gyr, and is denoted by the vertical black line in the spectrum. The corresponding wavelength of this peak is $0.62\,\mathrm{Gyr}^{-1} \approx 2\pi/10\,\mathrm{Gyr}^{-1}$. This is in fact the separation we would have estimated using equation (10) and corresponds to an estimated time since accretion of $\tilde{t}_{\mathrm{acc}} = 2\pi f_0 \approx 10\,\mathrm{Gyr}$. The rest of the peaks in the spectrum are associated to the harmonics of this wavenumber, i.e. $2f_0$, $3f_0$, etc.

The situation is similar when we consider a cut around $k_r = 0$. In this case, the scales present in the power spectrum are associated to separations in the Ω_ϕ direction. We find the peak with the highest amplitude to be at the same wavenumber f_0 and it is possible to distinguish some of its harmonics. However, due to the smaller number of streams we have in the Ω_ϕ direction the peaks are less clearly defined than for $P(k_r)$.

The Fourier method developed in this section may be considered to be very complementary to that introduced by MB08. Even if the gravitational potential is only approximately known, streams in frequency space will still distributed on a lattice (see below and section 4.3 of MB08). This implies that a Fourier analysis technique

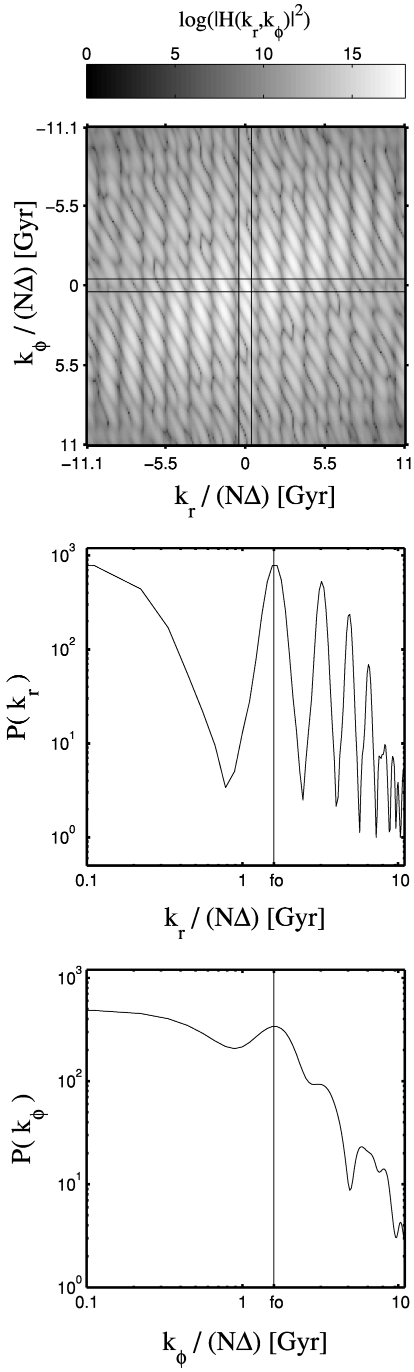

Figure 6. Top panel: the Fourier transform of the distribution of streams shown in the top-left panel of Fig. 5. The black lines denote the regions selected in the Fourier image to compute the one-dimensional power spectra, i.e. around $k_\phi = 0$ (middle panel) and $k_r = 0$ (lower panel). The black vertical lines in these panels show the location of the peak with the highest power in the spectrum.

will (always) provide an estimate of the time since accretion. Instead, in the presence of a very clear set of streams MB08's method can be used not only to provide a more accurate estimate of the time since accretion but also to narrow down the true underlying potential.

4 FREQUENCY SPACE FOR TIME-DEPENDENT POTENTIALS

In a hierarchical universe, the gravitational potentials associated to galaxies are expected to have changed over time. Under these circumstances, quantities such as the energy, apocentre and pericentre and also the frequencies of individual orbits will no longer be conserved. It is therefore of special interest to study how a time-dependent potential affects the structure of debris in frequency space.

To this end, we consider a simple model of a satellite accreted on to a Plummer sphere whose mass varies according to

$$M(t) = M_0 \exp(t/t_{\rm scale}), \tag{17}$$

where we explore several values for the time-scale, $t_{\rm scale}$. The growth in mass will lead to a shrinking of the possible orbits, and be manifested in an increase in the frequencies and acceleration experienced by the particles with time.

4.1 Time evolution of the frequencies and the rate of change of the potential

To derive the evolution of the frequencies of motion for an orbit in a time-dependent mass distribution such as that given by equation (17), we proceed as follows. At each step of this orbit's time integration, we take the instantaneous position and velocity as initial conditions to compute an orbit in the instantaneous (frozen) associated potential. Then, for this orbit we derive an instantaneous set of frequencies.

We will consider the evolution of two different orbits: an initially outer orbit with an apocentre of $r_{\rm apo} \approx 64$ kpc and pericentre of $r_{\rm per} \approx 19$ kpc, and a second inner orbit with $r_{\rm apo} \approx 25$ kpc and $r_{\rm per} \approx 5$ kpc. The initial values of the frequencies of the outer orbit are $\Omega_r \approx 8\,{\rm Gyr}^{-1}$ and $\Omega_\phi \approx 6\,{\rm Gyr}^{-1}$, whereas for the inner one they are $\Omega_r \approx 25\,{\rm Gyr}^{-1}$ and $\Omega_\phi \approx 13\,{\rm Gyr}^{-1}$. Both orbits are launched from their apocentre.

Let us first consider a slowly varying potential, where $t_{\rm scale} = 30$ Gyr. We follow the evolution of the orbit over 14 Gyr. The top panel in Fig. 7 shows the time evolution of the radial action J_r for this case, where black and light-grey lines in this figure correspond

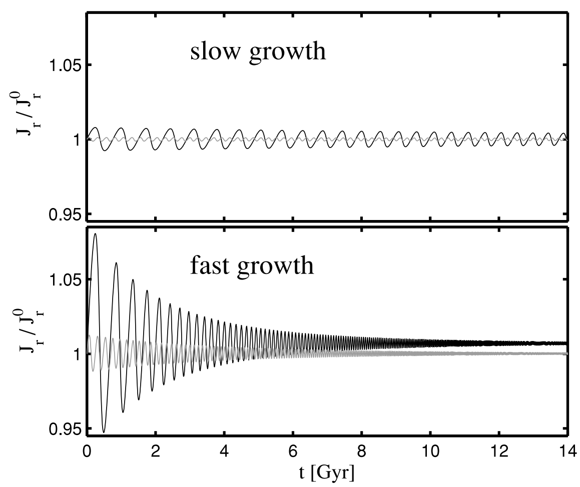

Figure 7. Time evolution of the radial action of two different orbits in a very slow (top panel) and a very fast (bottom panel) time varying Plummer potentials. The black and light-grey curves correspond to an outer and an inner orbit, respectively. The observed oscillatory behaviour is related to the orbital motion.

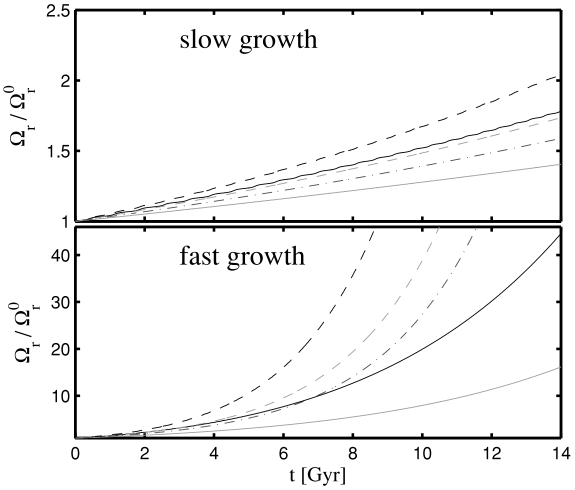

Figure 8. Time evolution of the radial frequency for two different orbits in a very slow (top panel) and a very fast (bottom panel) time varying Plummer potentials. The black and light-grey curves correspond to an outer and an inner orbit, respectively. The dashed lines represent the time evolution of the normalized energies of each orbit E/E_0, while the dot–dashed line shows the time evolution of the mass of the host M/M_0.

to the outer and the inner orbit respectively. This figure shows that the instantaneous action J_r displays an oscillatory behaviour,[1] with a period that corresponds to that of the orbit.

This is not surprising since under adiabatic variations of the potential it is the time average of the actions that remains constant (see Goldstein et al. 2001; Wells & Siklos 2006). In general, for a given orbit the amplitude of the oscillation depends on the time-scale on which the potential grows. By increasing $t_{\rm scale}$, the evolution is more adiabatic and the amplitude of the oscillation is decreased.

In order for an orbit to be in a condition of adiabatic invariance, it is necessary that $t_{\rm orb} \ll t_{\rm scale}$, where $t_{\rm orb}$ is the orbital period. Since inner orbits have shorter orbital periods, we expect those to behave 'more adiabatically' compared to outer orbits. This is demonstrated in the top panel of Fig. 7, where the amplitude of the oscillation of J_r is smaller for the inner orbit.

For the outer orbit in the rapidly growing potential, $t_{\rm scale} = 3$ Gyr, the amplitude of oscillation is larger, especially at early times when the orbit is farther away from the adiabatic regime (since its initial period, $T_r = 0.78$, is comparable to $t_{\rm scale}$). As the mass of the system grows in time, which leads to the deepening of the potential well, orbits are continuously driven towards deeper regions of the well, implying that the corresponding orbital periods decrease with time. Therefore, what we observe as the damping of the amplitude of oscillation is a transition from a non-adiabatic towards an adiabatic regime.

In Fig. 8, we focus on the evolution of the radial frequency Ω_r (the angular frequency Ω_ϕ depicts a qualitatively similar behaviour). The top and bottom panels of this figure correspond, respectively, to the slowly and the rapidly varying potentials. Note that in contrast to the actions the frequencies do change with time, and their evolution appears to follow closely that of the potential. For comparison, we plot in Fig. 8 the time evolution of the normalized energy of each orbit E/E_0 (dashed lines), and of the mass of the system M/M_0 (dot–dashed line).

[1] Note that due to the spherical nature of the potential the other two actions, associated with the angular momentum, remain constant in time.

The exact relation between the evolution of the frequencies and that of the potential cannot be derived analytically in the general case. However, some insights may be obtained from two simple cases: the homogeneous sphere and the Kepler potentials.

For the homogeneous sphere, the radial period $T_r \propto \rho^{-\frac{1}{2}}$ or $T_r \propto M^{-\frac{1}{2}}$ (Binney & Tremaine 2008), therefore $\Omega_r \propto M^{\frac{1}{2}}$. Hence, for $M(t) \propto \exp(t/t_{\rm scale})$ we obtain

$$\Omega_r(t) \propto \exp(t/2t_{\rm scale}). \tag{18}$$

Therefore, the frequencies evolve in time with the same functional form as the potential, but on a time-scale that is twice as long. Consequently, their evolution is slower.

In a Kepler potential, the radial orbital frequency of a particle can be expressed in terms of its actions as (Binney & Tremaine 2008, appendix E)

$$\Omega_r = \frac{(GM)^2}{(J_r + L)^3} \tag{19}$$

and therefore

$$\Omega_r(t) \propto \exp(2t/t_{\rm scale}). \tag{20}$$

Again, in this example we find that frequencies are evolving in a similar fashion as the potential. Therefore, a very external orbit in the Plummer sphere should initially evolve at a rate similar to that given by equation (20) (as for the Kepler potential). On the other hand, inner orbits should evolve at a rate similar to that of the homogeneous sphere. Thus, we can already see that orbits in a given potential will evolve at different rates, depending on their initial location in phase space.

4.2 Structure in frequency space

In this section, we address how the debris of a satellite is distributed in frequency space in the time-dependent Plummer potential discussed above.

We ran simulations with the same satellite and orbital initial conditions as described in Section 3.2.2. We followed its evolution in the Plummer potential with two different time-scales, namely $t_{\rm scale} = 3$ and 12 Gyr. As before, we do not include the self-gravity of the satellite.

Fig. 9 shows the distribution of particles inside a sphere of 4 kpc radius located at ≈10kpc from the centre of the system after 10 Gyr of evolution. The top panel presents the results for $t_{\rm scale} = 12$ Gyr while the bottom panel corresponds to $t_{\rm scale} = 3$ Gyr. As we can see from this figure, even in a time-dependent system, satellite debris at a given spatial location is distributed in a regular pattern of patches in the space of orbital frequencies.

In the simulation where the time evolution is slow (i.e. $t_{\rm scale} =$ 12 Gyr), some of the structures may be decomposed into two clumps. As we explained in Section 3.2.2, such structures appear when neither the apocentre nor the pericentre of the orbits falls inside the sphere under consideration. In contrast, when the potential evolves quickly the particles in each stream are all distributed in compact single structures. This is because in this case the orbits have shrunk so much after 10 Gyr that all streams present in this volume have their apocentres inside the chosen sphere.

Comparison to the case in which the potential is fixed (Fig. 5) shows that streams in the Ω_r direction are not exactly distributed along a line of $\Omega_\phi =$ constant but rather on a line with a given curvature. This is due to the fact that orbits with different initial frequencies evolve at different rates (as discussed in the previous section). The amount of curvature observed in this space (e.g. Fig. 9)

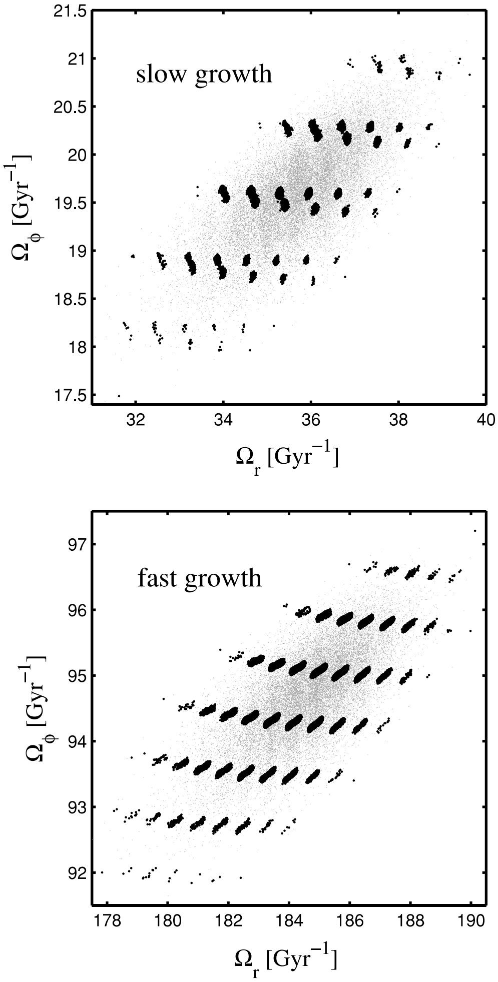

Figure 9. Distribution of particles in frequency space located inside a sphere of 4 kpc radius at ≈10 kpc from the centre of the time-dependent Plummer sphere after 10 Gyr of evolution. The time-scales for the mass growth of the Plummer sphere are $t_{\rm scale} = 12$ Gyr (top panel) and $t_{\rm scale} = 3$ Gyr (bottom panel). Note that structure in frequency space is not destroyed by the time varying nature of the potential.

depends on the rate of evolution of the potential. This is schematically depicted in Fig. 10. Particles located close to the homogeneous sphere regime will evolve at rates $\sim(2t_{\rm scale})^{-1}$, while those with orbits closer to the point-mass distribution regime will evolve at rates more similar to $2/t_{\rm scale}$, i.e. four times faster. Note that since the particles in the Plummer sphere occupy a smaller region in frequency space than that delimited by these two regimes, the difference in their rate of evolution will typically be smaller than the estimate just provided. If by the final time $t_{\rm end}$ the particles satisfy the condition $\int_{t_0}^{t_{\rm end}} \Delta\Omega_r(t){\rm d}t = 2\pi N$ their associated streams will be located along a curve roughly as depicted in this figure.

Note that the extent of the distribution of particles in frequency space has also changed, but since this is also dependent on the initial internal properties of the satellite it cannot be used to directly measure the evolution of the potential.

We may conclude from these experiments that the time evolution modelled here for the host potential does not destroy the coherence of satellite debris in frequency space. Furthermore, since the frequencies evolve at different rates even for particles with same origin, it may be possible to recover the evolution of the host potential by measuring the curvature of the lines over which the streams are

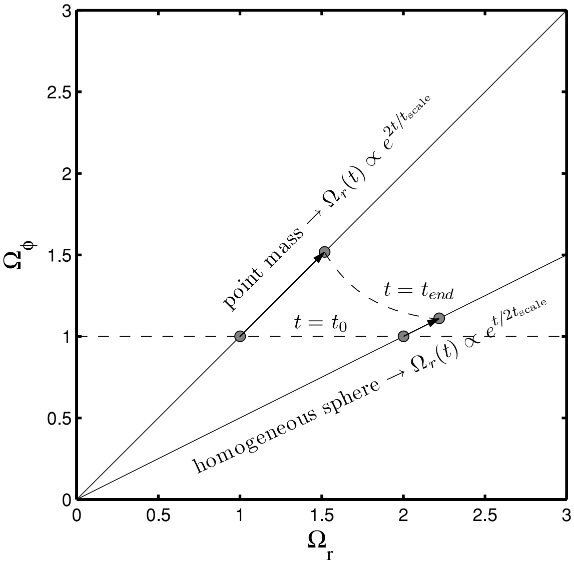

Figure 10. Schematic of the time evolution of the frequencies of two particles and their dependence on location in frequency space. At initial time, $t = t_0$, both particles have the same initial Ω_ϕ but different Ω_r. The frequency of the particle closer to the homogeneous sphere regime evolves at a slower rate than that which is closer to the point-mass distribution. This results in a lattice that has curvature in frequency space for those particles which satisfy $\int_{t_0}^{t_{\rm end}} \Delta\Omega_r(t)\,{\rm d}t = 2\pi N$, similar to that seen in Fig. 9.

distributed in frequency space. Note that this implies that the host's evolution has left its imprints in the present-day orbits of accreted stars. This is in contrast to the results by Peñarrubia et al. (2006) (see also Warnick, Knebe & Power 2008), who find that present-day observables only constrain the present-day mass distribution of the host, independent of its past evolution.

4.3 Estimating the time of accretion

The top panel in Fig. 11 shows the results of applying a two-dimensional Fourier transform to an image created from the distribution of streams shown in the top panel of Fig. 9. This corresponds to the satellite accreted 10 Gyr ago on to a host whose mass increases on $t_{\rm scale} = 12$ Gyr. As before, we compute the power spectrum along the k_ϕ and k_r directions. The middle panel shows $P(k_r)$, and the black line here denotes the location of the peak with the highest amplitude, having a wavenumber of $f_0 = 1.46$ Gyr. From this spectrum, we would estimate the satellite was accreted 9.2 Gyr ago. When $P(k_\phi)$ is considered, the highest amplitude peak is located at a wavenumber $f_0 = 1.36$ Gyr, corresponding to an estimated time of accretion of 8.6 Gyr. Therefore, in this example the analysis of the power spectrum suggests different times of accretion depending on whether Ω_r or Ω_ϕ is considered. Both values are reasonably close to the actual accretion time (10 Gyr ago), but the direction associated to Ω_r appears to provide a better estimate.

Fig. 12 shows the same result but now for the satellite accreted on to a host potential that evolves on $t_{\rm scale} = 3$ Gyr. $P(k_r)$ peaks at a wavenumber $f_0 = 1.4$ Gyr, as shown by the black line in the middle panel of this figure while $P(k_\phi)$ peaks at a wavenumber $f_0 = 1.21$ Gyr. The corresponding estimated times of accretion $\tilde{t}_{\rm acc}$ are 8.8 and 7.6 Gyr ago, respectively. Note that even though the potential evolves on a very short time-scale the estimated accretion times only differ by ∼15–25 per cent from the true value.

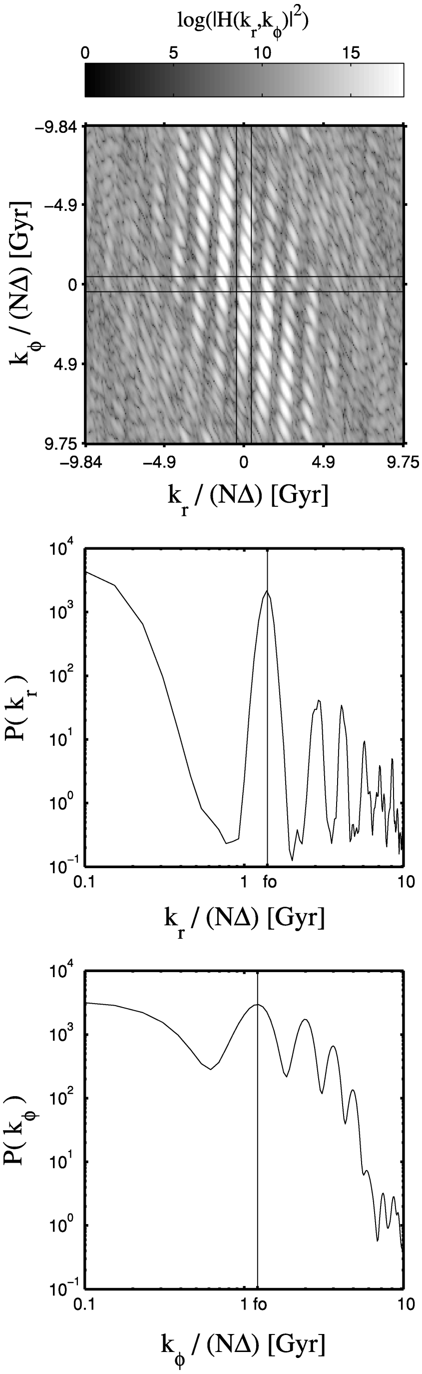

Figure 11. Top panel: the Fourier transform of the distribution of streams shown in the top panel of Fig. 9. As in Fig. 6, the middle and central panels depict the one-dimensional power spectra along the k_r and k_ϕ directions, respectively. The location of the first peak (denoted by the vertical lines in these panels) can be used to estimate the accretion time of the satellite.

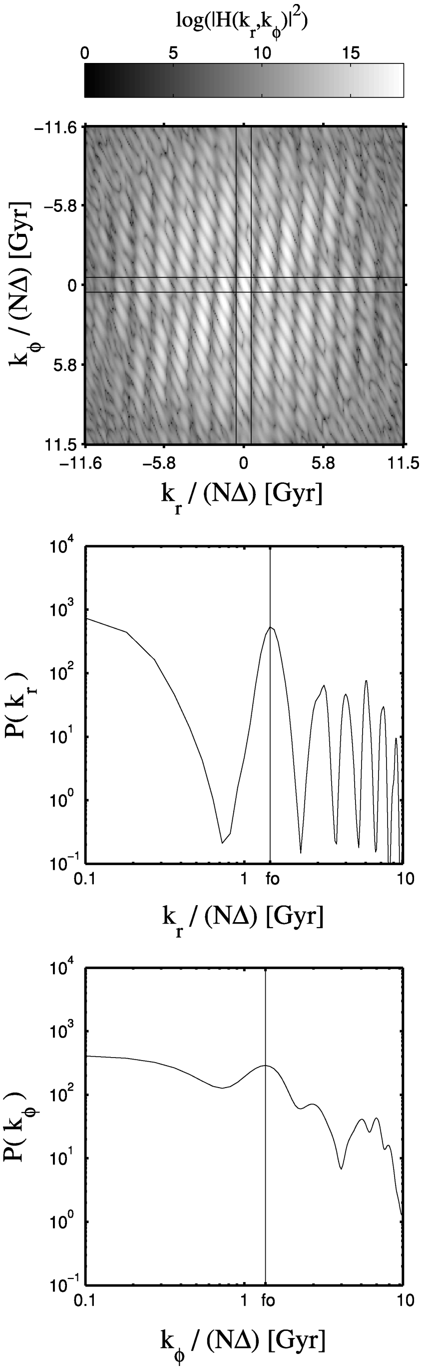

Figure 12. As in Fig. 11, now for the distribution of streams shown in the bottom panel of Fig. 9.

We may estimate the relation between the true time since accretion $t_{\rm acc}$ and $\tilde{t}_{\rm acc}$ for a general time-dependent potential as follows. Let us consider two particles that at final time are found in adjacent streams. As discussed before, the condition for this to happen is $\Delta\theta_i(t_{\rm acc}) = \int_0^{t_{\rm acc}} \Delta\Omega_i(t){\rm d}t = 2\pi$, for $i = r, \phi$. This implies

$$\int_0^{t_{\rm acc}} \Delta\Omega_i(t){\rm d}t = \Delta\Omega_i(t_{\rm acc})\tilde{t}_{\rm acc}. \qquad (21)$$

We may use the second mean value theorem for integration (Courant 1998), i.e. $\int_a^b G(t)\varphi(t)\,{\rm d}t = G(a)\int_a^x \varphi(t)\,{\rm d}t + G(b)\int_x^b \varphi(t)\,{\rm d}t$. If we take $\varphi(t) = 1$ and $G(t) = \Delta\,\Omega_i(t)$ then

$$\int_0^{t_{\rm acc}} \Delta\Omega_i(t)\,{\rm d}t = \Delta\Omega_i(0)t_{\rm g} + \Delta\Omega_i(t_{\rm acc})(t_{\rm acc} - t_{\rm g}),$$

where $t_{\rm g} \in (0, t_{\rm acc})$. Therefore, in equation (21)

$$\tilde{t}_{\rm acc} = t_{\rm acc} - t_{\rm g}[1 - \Delta\Omega_i(0)/\Delta\Omega_i(t_{\rm acc})], \qquad (22)$$

which shows that our estimate is always a lower limit to the actual time since accretion. Its accuracy depends on the particular form of the gravitational potential and on its evolution [through the quantities $\Delta\Omega_i(t_{\rm acc})$ and $t_{\rm g}$].

We have also performed an experiment in which an axisymmetric thin disc was grown adiabatically inside an initially spherical (Plummer) mass distribution. Therefore, in this case, both the shape and the depth of the gravitational potential have changed with time. We find that also under such conditions we are able to estimate the time of accretion with similar accuracy.

5 FULL *N*-BODY CASE

The previous analysis has shown that frequency space is particularly well suited for identifying streams from mergers, at least for the idealized potentials considered thus far. We now explore a more realistic case, namely that of a minor merger with a live host. We use one of the simulations of Villalobos & Helmi (2008, hereafter VH08), that model the formation of a thick disc via the merger of a relatively massive satellite on to a pre-existing thin disc. Two important physical processes take place during the merger which may affect the structure of the debris in frequency space. First, the satellite suffers significant dynamical friction. Secondly, the host system responds strongly to the perturber, resulting in a disc that has been significantly tilted and heated. This implies that, even though the total mass of the system is conserved, its distribution evolves in time. The VH08 simulation that we consider here corresponds to a two-component satellite (stars + dark matter) launched on a 30° inclination orbit with respect to the disc from a distance of approximately 84 kpc (∼50 disc scalelengths). The host consists of a (live) dark halo and a (live) thin disc. The total (and the stellar) mass ratio between the satellite and the host is 20 per cent. After 4.5 Gyr of evolution, the satellite is fully disrupted and has deposited debris in the disc of the host. The host disc is significantly thickened by this process and shows characteristics typical of thick discs.

5.1 Computing the frequencies

The remnant system modelled by VH08 does not have a separable gravitational potential which prevent us from deriving explicitly the action-angle variables using equation (2) and (3). Nevertheless, several methods have been developed to obtain the frequencies of orbits in general potentials. Here, we focus on the spectral analysis approach, introduced by Binney & Spergel (1982), which relies on the numerical integration of the equations of motion in a given potential. The basic idea is to perform a Fourier transform of the time series $\boldsymbol{x}(t)$ (i.e. the orbit), and then to derive the frequencies of motion.

To obtain a reliable Fourier spectrum, the orbits must be integrated for a very large number of periods. However, in the problem under consideration the orbits are not stationary, i.e. the frequencies are time dependent and so this approach cannot be applied directly using the orbits from the *N*-body simulation. This is why we have used the final output of the simulation to define a set of initial conditions which we integrate in a fixed (static) potential. This potential should resemble that of our simulation, and for simplicity we have taken a two-component model, consisting in a Miyamoto–Nagai disc (Miyamoto & Nagai 1975)

$$\Phi_{\rm disc} = -\frac{GM_{\rm disc}}{\sqrt{R^2 + (a + \sqrt{z^2 + b^2})^2}} \tag{23}$$

and NFW dark matter halo (Navarro, Frenk & White 1996)

$$\Phi_{\rm halo} = -\Phi_0 \frac{r_s}{r} \log\left(1 + \frac{r}{r_s}\right). \tag{24}$$

We have set the parameters of the model to $M_{\rm disc} = 2.5 \times 10^{10}\,{\rm M}_\odot$, $a = 1.8$ kpc and $b = 0.6$ kpc; $\Phi_0 = 1.05 \times 10^5$ km^2 s^{-2} and $r_s = 14.1$ kpc. These choices lead to a potential energy distribution that differs by at most 5 per cent from the true potential up to a radius of 50 kpc on the $z = 0$ plane. This radius is large enough to enclose the apocentres of 99 per cent of the particles presently found in a volume resembling the solar neighbourhood. We thus integrate the orbits of the stellar particles located in such a volume for approximately 100 orbital periods and compute their frequencies using the code developed by Carpintero & Aguilar (1998).

Note that the results are not strongly dependent on our particular choice of the potential, since substructure in integrals of motion space (Helmi & de Zeeuw 2000; Helmi et al. 2006) and in frequency space (MB08) are both robust to small differences in the mass distribution. This is because we always focus on small volumes in space and hence small changes in the potential essentially act as a zero-point offset, affecting all particles present in this volume in the same way.

5.2 Results

In Fig. 13, we present the distribution of stellar particles inside a sphere of 2 kpc radius located at 8 kpc from the centre of the remnant galaxy in some commonly used spaces to identify substructure. Here, the red particles represent those originally present in the disc, while those from the satellite are colour coded in black. The total number of stellar particles inside this sphere is approximately 27 000, out of which 23 000 belong to the satellite and 4000 to the host.[2]

The top panel of Fig. 13 shows the distribution of particles in the Ω_ϕ versus Ω_r space. Note the large amount of substructure present. As expected, satellite particles are distributed in multiple lumps associated with the different streams crossing this volume. These lumps are better defined for orbits which spend most of their time far from the centre, and so are found at low frequencies and have long mixing time-scales.

The upper envelope defined by the smallest Ω_r at a given Ω_ϕ corresponds to particles with low eccentricity (i.e. on more circular orbits) as discussed in Section 3.2.1. In our simulation, this region is preferentially populated by disc particles.

In general, orbits in axisymmetric potentials have three independent frequencies: the previously discussed Ω_r and Ω_ϕ and a third frequency associated with the vertical motion, Ω_z. However, particles in the thick disc typically have very short periods in the vertical direction. Hence, the number of streams expected in the Ω_z direction is very large and therefore it is hard to resolve in our simulation, and not discussed further here.

In the bottom-left panel of Fig. 13, we can observe the distribution of particles in the space defined by orbital apocentre and pericentre. The stripy features along lines of different eccentricities are the counterparts of the lumps located on diagonal lines in frequency space. The middle panel shows the $E-L_z$ space, where extended structures with slightly different orientations may be seen. The panel on the right shows a projection of velocity space, which clearly exhibits less well-defined structures in comparison to the other spaces discussed. In general, we may conclude from this figure

[2] This is due to higher number of particles used to simulate the satellite to properly resolve its structure in phase space. Therefore, in practice only 1 in 50 satellite particles should be considered.

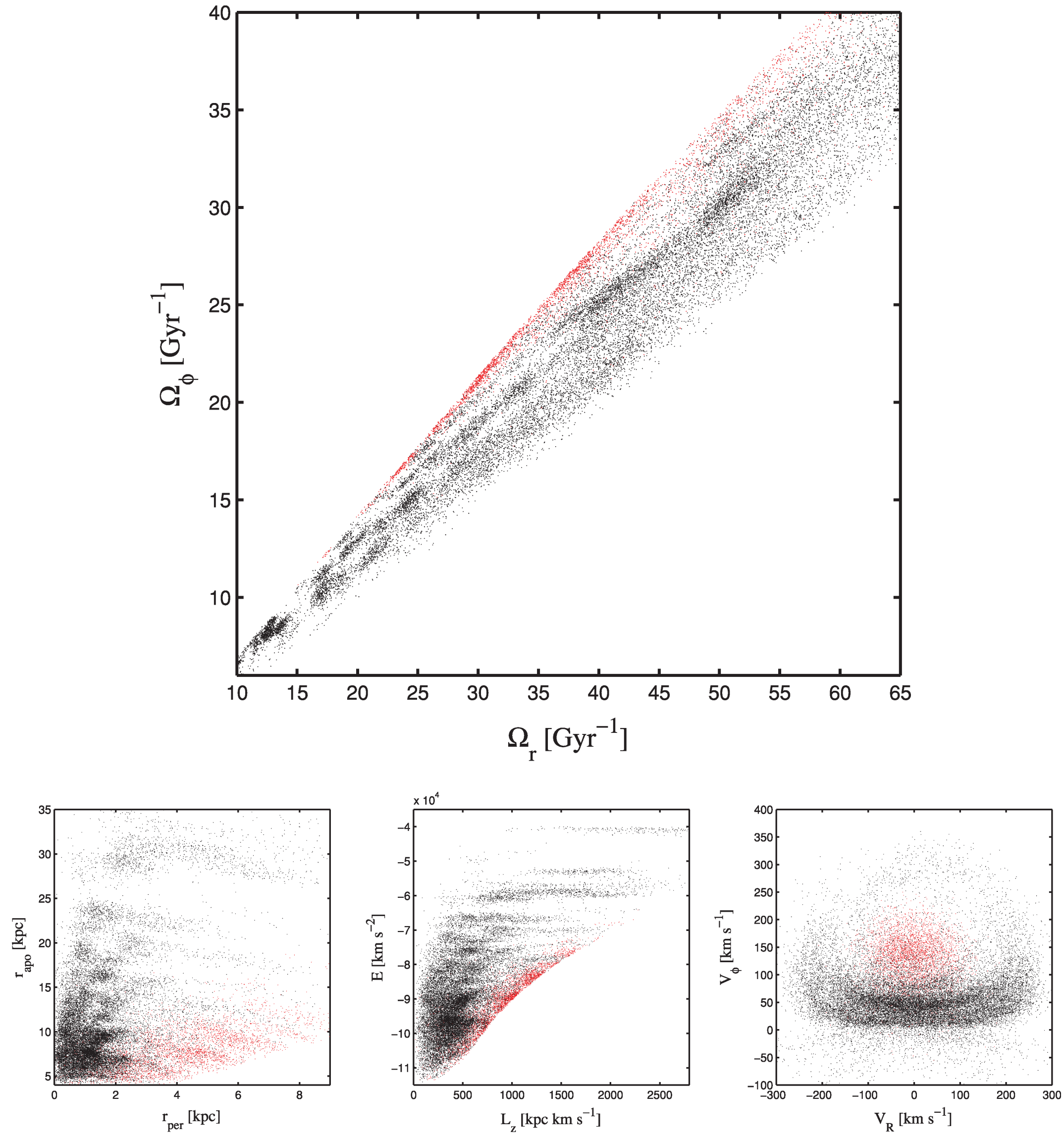

Figure 13. Distribution of stellar particles inside a sphere of 4 kpc radius located at 8 kpc from the centre of the remnant of a 5:1 merger between a satellite and a disc galaxy, after 4.5 Gyr of evolution. In all panels, the black dots represent particles from the satellite and red dots particles from the disc. The top panel shows the distribution of particles in frequency space, whereas the bottom panels correspond to the apocentre versus pericentre space (left-hand panel), the $E - L_z$ (middle panel) and the $V_R - V_\phi$ (right-hand panel) projections. Note that streams are much better defined in frequency space than in these other projections.

that streams are much better defined and easier to interpret in frequency space than in any of the other projections considered.

5.3 Estimating the time of accretion

In comparison with the idealized cases discussed in Sections 3.2.2 and 4.2, the distribution of particles in frequency space for the VH08 simulation is less regular. Nevertheless, we would like to explore if it is still possible to obtain a good estimation of the time of accretion of the satellite, using the Fourier analysis described in previous sections.

The top panel of Fig. 14 plots the image in Fourier space of the frequency plane Ω_ϕ versus Ω_r discussed above. This image was obtained by making a grid in frequency space and counting the number of particles in each grid element. As before, the black lines in the top panel of Fig. 14 denote the cuts around $k_r = 0$ and $k_\phi = 0$ made to compute the one-dimensional power spectra.

To estimate the uncertainties in the power spectrum, we create a second image obtained by assuming that the particles are spread throughout the permitted regions of frequency space according to a Poisson distribution. That is, we assign to each grid element N_p particles, where this number is drawn from a Poisson distribution with mean $\langle N \rangle = (N_{\rm disc} + N_{\rm sat})/n_{\rm grid}$, i.e. equal to average number of stellar particles per grid element. We then compute the Fourier transform of this distribution and the corresponding one-dimensional power spectra from the image. This procedure is repeated 1000 times, to yield an average power spectrum in each direction associated to a random distribution of particles in frequency space.

The results are shown in the bottom and middle panel of Fig. 14. The black solid line in each panel denotes the power spectrum

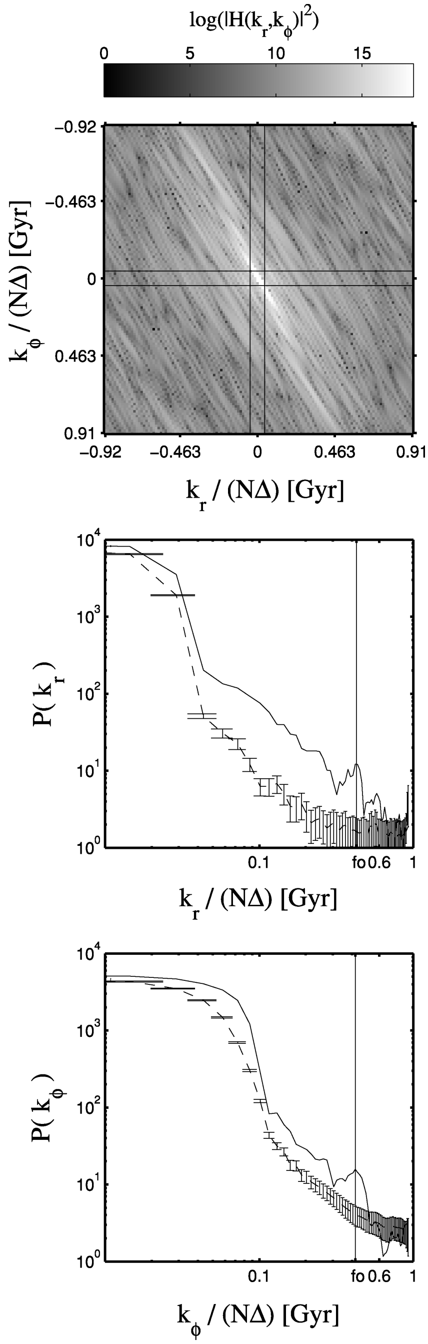

Figure 14. Top panel: the Fourier transform of the distribution of particles in frequency space shown in the top panel of Fig. 13. As in Fig. 6, the middle and central panels depict the one-dimensional power spectra around $k_\phi \sim 0$ and $k_r \sim 0$, respectively. The vertical lines in these panels show the location of the peak associated to the average separation between streams in frequency space, and can be used to estimate the accretion epoch. The dashed curve corresponds to the average power spectrum obtained from a random distribution of particles in frequency space. The error bars represent the rms dispersion from this average spectrum.

obtained from the actual distribution of particles in frequency space. The dashed line corresponds to the average power spectrum for our random distributions where the vertical error bars represent the rms dispersion around this average spectrum. As we can see, a statistically significant peak can be identified in the observed power spectrum along k_r (and also for k_ϕ). The wavenumber of this peak is $f_0 \approx 0.43$ Gyr for both the radial and angular directions. This corresponds to an estimated accretion time of 2.7 Gyr. Recall that this simulation is evolved for 4.5 Gyr. However, the satellite only starts to lose a significant amount of stars ~1 Gyr after infall (see fig. 3 of VH08). Therefore, we may conclude that the time since disruption of a satellite can be reasonably estimated even in a simulation with a live host.

6 DISCUSSION AND CONCLUSIONS

We have confirmed and extended previous work by MB08 showing that orbital frequencies constitute a very suitable space to identify debris from past accretion events. In this space, particles in a given volume of physical space are found to populate well-defined lumps, each of them associated with a different stream.

For time-independent potentials, these streams are distributed in a regular pattern along lines of constant frequency. As time goes by, the number of streams at a given physical location increases while the separation between adjacent streams decreases. We have shown here that this characteristic separation or scale can be used to estimate the time of accretion of the object through a Fourier analysis.

We have also addressed how the time evolution of the host affects substructure in frequency space. As an example, we have considered the case in which the mass of the host is increased exponentially in time on two different time-scales. We find that in contrast with the actions which are adiabatic invariants for slowly varying potentials, the frequencies always evolve in time, closely following the rate of change of the host potential. This evolution, however, does not destroy the clumpiness present in frequency space. Streams still look lumpy and are regularly distributed in this space, even if the host potential varies on a very short time-scale (when even the actions are no longer invariant). Interestingly, in this case, streams are not exactly distributed along straight lines of constant frequency but rather on lines whose curvature depends on the time-scale of growth of the potential. This implies that, contrary to previous claims (e.g. Peñarrubia et al. 2006; Warnick et al. 2008), the final distribution of streams does retain information on the evolution in time of the host.

Finally, we have analysed a full N-body simulation of the accretion of a satellite galaxy on to a disc galaxy. Due to the inclusion of other physical processes (such as self-gravity, dynamical friction and the variation in time of the distribution of mass in the system), the distribution of satellite particles in frequency space looks somewhat less regular than in the previously discussed idealized cases. Nevertheless, the space of frequencies is still rich in substructure associated to streams. Furthermore, even in this case Fourier analysis techniques can be used to estimate the time of accretion reasonably well, although in general, only a lower limit is obtained.

For all these examples, we have compared the final distribution of streams in the most commonly used spaces to identify satellite debris. These comparisons have shown that frequency space contains information that is either not present or is not simply obtained in other spaces. In general, streams are most sharply defined in frequency space.

One important simplification in our analysis is to consider the accretion of a single satellite galaxy. In reality, the process of the formation of a galaxy like the Milky Way will have involved many mergers (in the range of 5–40; see De Lucia & Helmi 2008). Therefore, it is possible, and even likely, that their debris will overlap in frequency space. However, as we have shown, the separation between adjacent streams in frequency space is predicted to be different for mergers that took place at different epochs. Moreover, the location of their debris in frequency space at the present time is dependent upon the initial orbital conditions. Consequently, we expect the overlap to be incomplete and hence the identification of their remnants to be feasible. We are currently analysing the full cosmological high-resolution N-body simulations of the Aquarius Project (Springel et al. 2008) in order to address this issue and to understand what to expect in the context of the hierarchical paradigm of structure formation.

ACKNOWLEDGMENTS

We are very grateful to Alvaro Villalobos for providing the simulation used in Section 5 and Daniel Carpintero for the software for the spectral analysis used in Section 5.1. FAG would like to thanks Saleem Zaroubi and Rajat Thomas for very helpful discussions. NWO is acknowledged for financial support through a VIDI grant to AH. We are indebted to the referee, Paul McMillan, for a through and insightful report that lead to improvements in the presentation and content of this paper.

REFERENCES

Antoja T., Valenzuela O., Pichardo B., Moreno E., Figueras F., Fernández D., 2009, ApJ, 700, L78
Arifyanto M. I., Fuchs B., 2006, A&A, 449, 533
Belokurov V. et al., 2006, ApJ, 642, L137
Binney J., Spergel D., 1982, ApJ, 252, 308
Binney J., Tremaine S., 2008, Galactic Dynamics. Princeton Univ. Press, Princeton, NJ
Bullock J. S., Kravtsov A. V., Weinberg D. H., 2000, ApJ, 539, 517
Carpintero D. D., Aguilar L. A., 1998, MNRAS, 298, 1
Courant R., 1988, Differential and Integral Calculus, Vol. 1, Wiley-Interscience, New Jersey
De Lucia G., Helmi A., 2008, MNRAS, 391, 14
Eggen O. J., 1996, AJ, 112, 1595
Font A. S., Johnston K. V., Bullock J. S., Robertson B. E., 2006, ApJ, 646, 886
Goldstein H., Poole C. P., Safko J. L., 2001, Classical Mechanics. Addison-Wesley, Massachusetts
Gould A., 2003, ApJ, 592, L63
Gould A., Salim S., 2003, ApJ, 582, 1001
Governato F. et al., 2004, ApJ, 607, 688
Governato F., Willman B., Mayer L., Brooks A., Stinson G., Valenzuela O., Wadsley J., Quinn T., 2007, MNRAS, 374, 1479
Grillmair C. J., 2006, ApJ, 645, L37
Helmi A., de Zeeuw P. T., 2000, MNRAS, 319, 657
Helmi A., White S. D. M., 1999, MNRAS, 307, 495
Helmi A., White S. D. M., de Zeeuw P. T., Zhao H., 1999, Nat, 402, 53
Helmi A., White S. D. M., Springel V., 2003, MNRAS, 339, 834
Helmi A., Navarro J. F., Nordström B., Holmberg J., Abadi M. G., Steinmetz M., 2006, MNRAS, 365, 1309
Hernquist L., 1990, ApJ, 356, 359
Ibata R. A., Gilmore G., Irwin M. J., 1994, Nat, 370, 194
Ibata R., Irwin M. J., Lewis G. F., Ferguson A. M. N., Tanvir N., 2003, MNRAS, 340, L21
Klement R. et al., 2009, ApJ, 698, 865
Klypin A., Gottlöber S., Kravtsov A. V., Khokhlov A. M., 1999, ApJ, 516, 530
Knebe A., Gill S., Kawata D., Gibson B. K., 2005, MNRAS, 357, 35
McMillan P. J., Binney J., 2008, MNRAS, 390, 429 (MB08)
Minchev I., Quillen A. C., Williams M., Freeman K. C., Nordhaus J., Siebert A., Bienayme O., 2009, MNRAS, 396, 56
Miyamoto M., Nagai R., 1975, PASJ, 27, 533
Moore B., Ghigna S., Governato F., Lake G., Quinn T., Stadel J., Tozzi P., 1999, ApJ, 524, L19
Navarro J. F., Frenk C. S., White S. D. M., 1996, ApJ, 462, 563
Navarro J. F., Helmi A., Freeman K. C., 2004, ApJ, 601, L43
Peñarrubia J., Benson A. J., Martínez-Delgado D., Rix H. W., 2006, ApJ, 645, 240
Perryman M. A. C. et al., 2001, A&A, 369, 339
Plummer H. C., 1911, MNRAS, 71, 460
Salim S., Gould A., 2003, ApJ, 582, 1011
Scannapieco C., White S. D. M., Springel V., Tissera P. B., 2009, MNRAS, 396, 696
Smith M. C. et al., 2009, MNRAS, 399, 1223
Springel V. et al., 2008, MNRAS, 391, 1685
Steinmetz M., Navarro J. F., 1999, ApJ, 513, 555
Yanny B. et al., 2003, ApJ, 588, 824
Yanny B. et al., 2009, ApJ, 137, 4377
Villalobos A., Helmi A., 2008, MNRAS, 391, 1806 (VH08)
Vogelsberger M., White S. D. M., Helmi A., Springel V., 2008, MNRAS, 385, 236
Warnick K., Knebe A., Power C., 2008, MNRAS, 385, 1859
Wells C. G., Siklos S. T. C., 2006, European J. Phys., 28, 105
White S. D. M., Rees M. J., 1978, MNRAS, 183, 341
Zwitter T. et al., 2008, AJ, 136, 421

This paper has been typeset from a TEX/LATEX file prepared by the author.